



# Generation of second harmonic Bessel beams through hybrid meta-axicons

HUA LONG,<sup>1</sup> LE NIU,<sup>1</sup> KAI WANG,<sup>1,3</sup>  WENCHAO ZHAO,<sup>1</sup>   
XUANMIAO HONG,<sup>1</sup> WEIWEI LIU,<sup>1</sup>  BING WANG,<sup>1</sup> AND PEIXIANG LU<sup>1,2,4</sup>

<sup>1</sup>Wuhan National Laboratory for Optoelectronics and School of Physics, Huazhong University of Science and Technology, Wuhan 430074, China

<sup>2</sup>Hubei Key Laboratory of Optical Information and Pattern Recognition, Wuhan Institute of Technology, Wuhan 430205, China

<sup>3</sup>kale\_wong@hust.edu.cn

<sup>4</sup>lupeixiang@hust.edu.cn

**Abstract:** Bessel beams are of great potential applications in many fields due to their non-diffraction and self-reconstruction. Here we firstly present a type of nonlinear meta-axicon to generate second harmonic Bessel beams. The nonlinear meta-axicons are based on Au/WS<sub>2</sub> hybrid nanostructures. Zero-order and first-order Bessel beams of second harmonic are generated under exciting of 810 nm femtosecond laser. In addition, the performances of the nonlinear meta-axicons, such as the second harmonic generation (SHG) efficiency, non-diffracting distance and full width at half maximum (FWHM) are analyzed theoretically and experimentally. The experimental results are consistent with the predicted, which can enable miniaturized nonlinear optical devices related to generate nonlinear Bessel beams, having potential application in nonlinear optical manipulation, imaging and tractor beams.

© 2020 Optical Society of America under the terms of the [OSA Open Access Publishing Agreement](#)

## 1. Introduction

Bessel beams play a critical role in many optical applications due to their interesting properties such as nondiffraction and self-reconstruction characteristics. Their transverse electrical intensity distribution remained invariant during propagation in free space, which is useful for various kinds of applications, including particle trapping, tractor beams, laser machine, and optical communications. To generate Bessel beams, some methods like axicons, cascading lens, metallic subwavelength metasurfaces have been used [1–6]. Among these methods, ultrathin subwavelength metasurfaces have drawn much attention due to their outstanding advantages [7–8]. Subwavelength metasurfaces with spaced phase shifters have been used to control the optical wavefront and propagation of light, leading to various compact optical components including lenses, holograms, and polarization-selective devices [9–15]. Both metallic and dielectric metasurface axicons have been reported to generate Bessel beam [16–18]. They have shown prominent advantages, such as small size, high numerical aperture and strong trapping force. Here we firstly present a type of nonlinear meta-axicon to generate second harmonic Bessel beams, realizing the frequency conversion and optical modulation in one single nano-optical device.

Nonlinear optics is the branch of optics which examines the light behavior in nonlinear materials. The nonlinear optical materials play an important role in many photonics applications, including photon generation, transmission, manipulation, and imaging [19–20]. Recently, nonlinear metasurfaces have attract much attention due to their local field enhancement effects at the nanoscale by surface plasmon excitation [21–22]. The nonlinearities of the nonlinear metasurfaces with plasmonic structure are reported to be significantly enhanced. In many reported nonlinear meta-surfaces, metal-based metasurfaces act as nonlinear signal generator

and phase modulator simultaneously. However, their applications are limited due to low SHG conversion efficiencies of metal materials (with  $\chi^{(2)} \sim \text{pm/V}$ ) [23–24]. In order to improve the nonlinear efficiencies of nonlinear metasurfaces, a type of hybrid nonlinear metasurfaces has been proposed by coupling the plasmonic metasurfaces to materials with giant nonlinear responses [25–28]. Here, we choose  $\text{WS}_2$  monolayers as the nonlinear materials ( $\chi^{(2)} \sim \text{nm/V}$ ) [29–30]. Then we present a nonlinear meta-axicon based on  $\text{WS}_2/\text{Au}$  hybrid structure to generate zero-order and first-order Bessel beams of SHG. The performances of the nonlinear meta-axicons are analyzed, such as the enhanced SHG responses, the non-diffracting distances and the FWHM of the generated nonlinear Bessel beams. The experimental results are consistent with the predicted results. These nonlinear meta-axicons have potential applications in nonlinear optical manipulation, imaging and tractor beams.

## 2. Theory and design

The electrical intensity distribution of the Bessel beams propagating along the  $z$  axis can be described in cylindrical coordinate by the following equation [17],

$$E(r, \phi, z) = A \cdot \exp(ik_z z) \cdot J_n(k_r r) \cdot \exp(\pm in\phi) \quad (1)$$

where  $A$  is the amplitude,  $k_r$  and  $k_z$  are the transverse and longitudinal wavevectors, respectively.  $J_n$  is the Bessel function of the first kind, and  $n$  is the Bessel function order. For  $k_r$  and  $k_z$ , the following equation is satisfied,

$$\sqrt{k_r^2 + k_z^2} = k = 2\pi/\lambda \quad (2)$$

where  $k$  is the wavevector,  $\lambda$  is the wavelength.

From Eq. (1) we can see that the transverse electrical intensity profiles of Bessel beams are independent of the  $z$  coordinate, indicating their non-diffracting characteristic. And higher-ordered Bessel beams ( $n > 0$ ) carry orbital momentum and have zero intensity along the  $z$  axis at  $r = 0$ .

Typical axicon is often used to generate zero-order Bessel beams, which is conically shaped lens, by refracting all incident plane waves symmetrically towards the optical axis. Using meta-axicons, the same goal can also be achieved. For instance, based on Pancharatnam-Berry phase method, the meta-axicon to generate a zero-order Bessel beam at SHG wavelength requires a phase profile  $\Psi(r)$  of a phase gradient along  $r$  direction as the followed, [17]

$$-\frac{2\pi}{\lambda_{SHG}} \sin \alpha = \frac{d\psi}{dr} \quad (3)$$

where  $\alpha$  is the refractive angle,  $\lambda_{SHG}$  is the wavelength of SHG. From the generalized Snell's law [31], we can predict that all light rays will be refracted with the same angle  $\alpha$  at the wavelength of SHG through this meta-axicon.

Here, we also can write the above condition as followed [32],

$$k_{SHG} \cdot \sin \alpha = -\frac{2\pi}{\Gamma} \quad (4)$$

where  $\Gamma$  is the spatial period of the full rotation angle variation along  $r$  direction,  $k_{SHG}$  is the wavevector at SHG wavelength. In our experiments, we use the phase profile in Cartesian coordinates as followed to generate SHG zero-order Bessel beam,

$$\psi(x, y) = 2\pi - (2\pi/\lambda_{SHG}) \cdot \sqrt{x^2 + y^2} \cdot 0.9 \quad (5)$$

where  $x$  and  $y$  are the Cartesian coordinates of each nanohole on the metasurface, satisfying the relationship of  $x^2 + y^2 = r^2$ . Here, we choose  $\lambda_{SHG}$  wavelength at 405 nm. Then we obtain

the corresponding phase distribution. In our metasurfaces, the phase profile is imparted by the rotation of each gold nano-hole at a position  $(x, y)$  by an angle  $\theta$ , which is defined as the angle between the long-axis of the rectangular gold nanohole and x axis in the labor frame.

In addition, to generate a first-order Bessel beam, we use the phase profile as followed [17],

$$\psi(x, y) = 2\pi - (2\pi/\lambda_{SHG}) \times \sqrt{x^2 + y^2} \times 0.9 + \phi \quad (6)$$

where  $\phi = \arctan(y/x)$  is the azimuthal phase. The phase profile undergoes rotation from 0 to  $2\pi$  through the azimuthal direction.

Figures 1(a) and 1(b) show schematic sketch of our nonlinear meta-axicon structure and the generation of SHG Bessel beam through the nonlinear meta-axicon. The nonlinear meta-axicon are composed of two components, one is the gold nanohole arrays. The other is the monolayer  $WS_2$  covering on the gold nanohole arrays. For the hybrid nonlinear meta-axicons, the phase distribution of the emitted SH signal is modulated by designing the rectangular gold nanohole with different oriental angle,  $\theta$ , see Fig. 2(a). The gold nanohole is with length of 185 nm (L) and width of 80 nm (W). The size of unit cell is 330 nm. R is the diameter of the nanoholes array region. Under the exciting of the normal incident fundamental plane waves at 810 nm, a non-diffracting SHG beam are generated through the nonlinear meta-axicon, with the non-diffracting distance of  $Z_{max}$  and a refractive angle,  $\alpha$ .

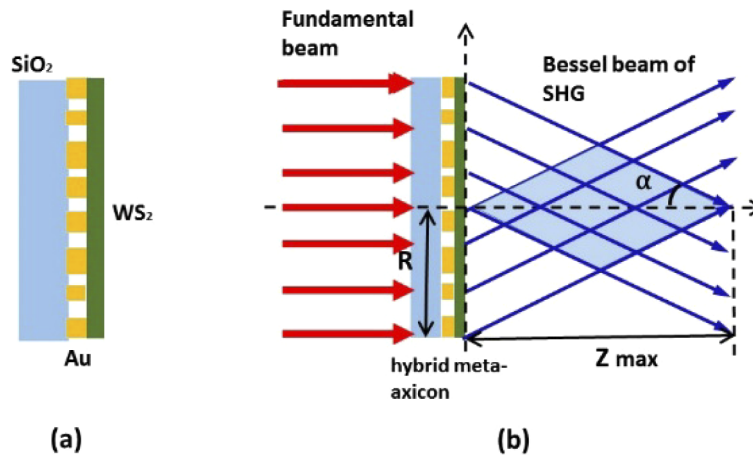


**Fig. 1.** The schematic sketch of (a) the Au/ $WS_2$  hybrid nonlinear meta-axicon and (b) the generation of SHG Bessel beam through the nonlinear meta-axicon

In linear metasurfaces, the phase profile is imparted by the rotation of  $\theta$ . As we know, when a left circular polarized (LCP) fundamental beam passes through the rectangular gold nanohole, the transmitted fundamental beam with a right circular polarized (RCP) is delivered by a geometric phase delay of  $2\theta$ . However, in our nonlinear metasurfaces, two incident fundamental photons are with geometric phase of  $2\theta$  after passing through the Au nanoholes. Therefore, through SHG processing passing through the  $WS_2$  monolayer, the output second harmonic photon is with the geometric phase of  $4\theta$  [32]. According to the above equations, we use the distribution of  $4\theta = \Psi$  in hm the hybrid metasurfaces to acquire SHG Bessel beams. The spatial period of the full rotation angle variation,  $T$ , is set to be  $0.889 \mu\text{m}$  for our metasurfaces. Then we predict the refractive angle  $\alpha$  of the nonlinear meta-axicon is  $26.7^\circ$ .

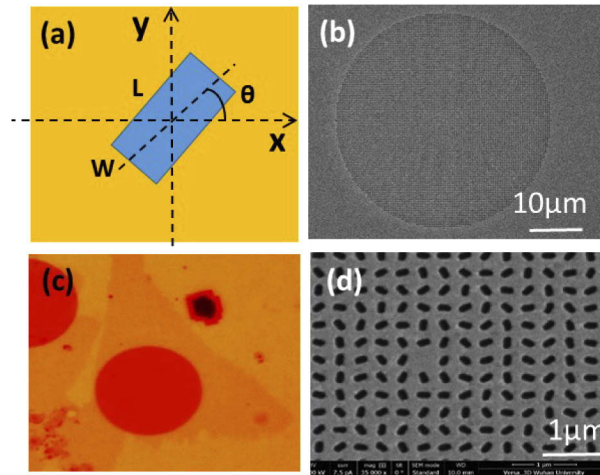


**Fig. 2.** (a) The geometry of the unit cell of the designed Au metasurfaces. The size of unit cell is 330 nm. The nanohole has length of  $L = 185$  nm and width of  $W = 80$  nm, and it rotates in the  $x$ - $y$  plane with an orientation angle,  $\theta$ . (c) The optical image of  $\text{WS}_2/\text{Au}$  hybrid metasurface. (b) and (d) SEM images of the Au nanohole arrays.

### 3. Experimental

The fabrication method of  $\text{WS}_2$ -Au hybrid nonlinear meta-axicons has been described in detail [28]. Firstly, a gold nanoholes array is obtained by focused ion beams method on gold thin films, which has been deposited on quartz substrate by electron beam evaporation. The thickness of the gold nanoholes array is 60 nm. Then we transfer  $\text{WS}_2$  monolayers from sapphire substrates onto the gold nanoholes array using polymethyl methacrylate (PMMA) film, with the help of an optical microscope. Finally, the  $\text{WS}_2$ -Au hybrid meta-axicons are obtained after removing the PMMA film on  $\text{WS}_2$ .

Figures 2(b) and 2(d) show scanning electron microscope images of the fabricated gold nanoholes array. We can see the rectangular nanoholes with varied orientations. Figure 2(c) exhibits the optical microscope image of  $\text{WS}_2/\text{gold}$  nanoholes hybrid metasurface. From this figure, we can see the gold nanohole array is fully covered by the  $\text{WS}_2$  monolayer.

Figure 3 shows the schematic sketch of the imaging system, which is used to measure the second harmonic (SH) signal profiles and the SHG spectra from the hybrid metasurfaces. In this system, a mode-locked Ti-sapphire femtosecond laser (Virtara Coherent, 8 fs and 80 MHz,

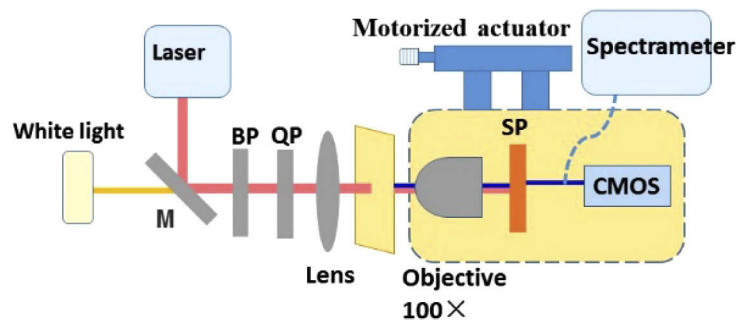


**Fig. 3.** The schematic sketch of the experiment setup for the emitted second harmonic signal profiles and the SHG spectra measurements.

810 nm) is used as the fundamental beam source [33]. The incident laser becomes circular polarized after passing through the polarizer (BP) and quarter-wave plate (QP). Then the circular polarized beam irradiates on the nonlinear metasurfaces by a lens. Through the hybrid nonlinear meta-axicon a non-diffracting Bessel beams at 405 nm are generated. The SHG emission from the sample with opposite circular polarization is collected by an objective lens (Olympus, 100× and 0.95 NA). The distance between the objective and the nonlinear metasurfaces is adjusted by a motorized actuator through moving the objective lens. Finally, the SHG signal is detected by a complementary metal oxide semiconductor (CMOS) camera or a spectrometer (Princeton Instruments Acton 2500i with Pixis CCD camera).

#### 4. Results and discussion

To verify the efficiency of this hybrid nonlinear metasurfaces, we measured the SHG signal of the hybrid nonlinear metasurfaces, the bare Au metasurfaces and the monolayer WS<sub>2</sub> under the same experimental condition (the incident laser power is about 80 mW). We find that for the bare Au metasurfaces, no SHG signal is detected. The SHG spectra obtained from the hybrid metasurface and the WS<sub>2</sub> monolayer are compared in Fig. 4(a). We can observe peaks with center wavelength of 405 nm, indicating much higher SHG efficiency than the bare gold metasurface. And the SHG intensity of the hybrid metasurfaces is improved about 9 times than that of the bare WS<sub>2</sub> monolayer due to the local field enhancement effects of SHG [34–35]. The SHG efficiencies of the bare WS<sub>2</sub> monolayer and the hybrid metasurfaces are measured to be  $\sim 10^{-7}$  and  $\sim 10^{-6}$ , respectively. To analyze this enhancement effect, the electric field distribution near the interface between Au nanoholes and WS<sub>2</sub> monolayer is simulated using finite-difference time-domain (FDTD) methods. In the simulated model of the metasurfaces, the size of the unit cell and the gold nanohole are the same with our fabricated samples. The thickness of the gold film and the SiO<sub>2</sub> substrate is 60 nm and 100 nm, respectively. Considering the influences of the orientation of the hole, the absorption spectra and the electric distribution of two units with different oriental holes are simulated. One is with  $\theta=45^\circ$ . The other is with  $\theta=0^\circ$ . Figure 4(b) show the simulated absorption spectra, with incident circular polarized plane wave. The dashed curve is the measured spectra with the gold nanoholes array under the illumination of a non-polarized white light. It can be seen that the absorption peaks obtained in simulation locate near the peaks measured. We can see the surface plasmon resonance located near 810 nm for the two units, which benefit for the enhancement of SHG. And a slight difference of the transmittance is observed between the two units, indicating a slight influence of the holes direction on the transmitted power of fundamental light. The electric field distributions in the transmitted wave are examined for a normally incident wave at 810 nm. And the incident electric field intensity is set to be 1. Figures 4(c) and 4(d) show the corresponding simulated electric field distribution at 810 nm for the two units with different oriental holes with  $\theta=45^\circ$  and  $\theta=0^\circ$ , respectively. The electric field intensity distribution is monitored in xy plane at the interface of Au and air. In the figures we can see enhanced electric field ( $E^2$ ) near the Au/air interface in both units. These results are consistent with the predicted. To compare the enhancement effect of different holes with different orientation, we calculate the averaged enhancement factor of  $E^2$  in the region near the holes (a concentric square region with side length of 200 nm). The averaged enhancement factors of  $E^2$  are 9.3 and 8.1 for the nanoholes with  $\theta=0^\circ$  and  $\theta=45^\circ$ , respectively. So small differences of the enhancement effects is obtained between the two units, which will induce small differences of SHG intensity near the different oriented holes excited by circular polarized light.

The SHG zero-order Bessel beams through two hybrid meta-axicons with  $R = 15 \mu\text{m}$  and  $R = 20 \mu\text{m}$  are measured. The electric field distributions in the transmitted wave are examined for a normally incident wave at 810 nm. The SHG images at the different planes from 0 to 50  $\mu\text{m}$  along the z-axis are captured. The intensity distribution on xz plane of the two nonlinear metasurfaces are shown in Figs. 5(a) and 5(b), respectively. We can see the non-diffracting

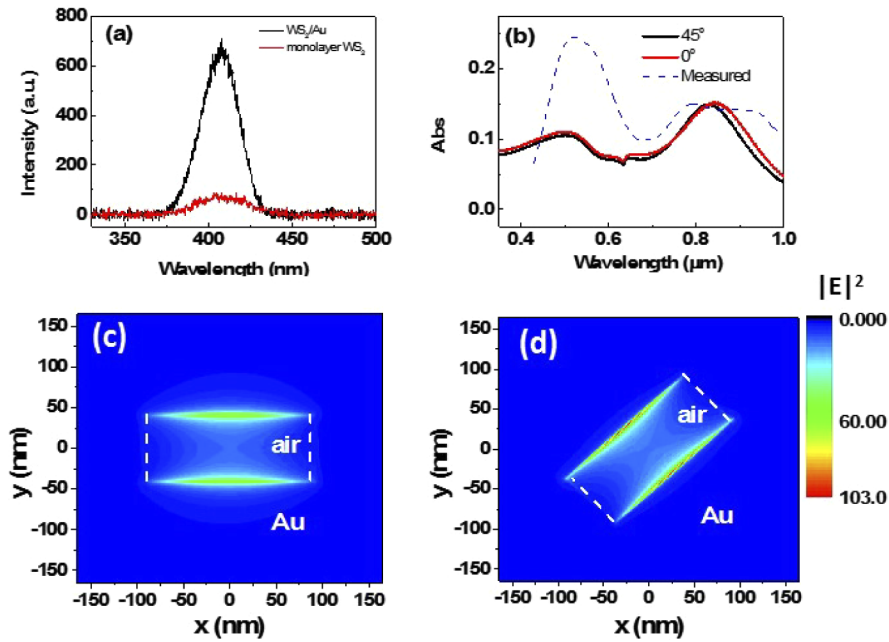


**Fig. 4.** (a) SHG enhancement in the hybrid metalens. Comparison of the SHG spectra of WS<sub>2</sub>/Au hybrid metasurface and the bare WS<sub>2</sub> monolayer. (b) The simulated absorption spectra of the unit cell structure with different oriental nano-holes of  $\theta=0^\circ$  and  $\theta=45^\circ$ , excited by circularly polarized fundamental beams. The dashed curve is the measured spectra with the nanoholes array. (c) and (d) The simulated electric field distribution on the intersurface of Au and air, for nanoholes of  $\theta=0^\circ$  and  $\theta=45^\circ$ , respectively. Excited by 810 nm plane wave.

propagated beams along  $z$  direction. It is worth noting that an ideal Bessel beam should be generated from an infinitely large lens, which is impossible to be implemented practically. So the non-diffracting distance is limited.

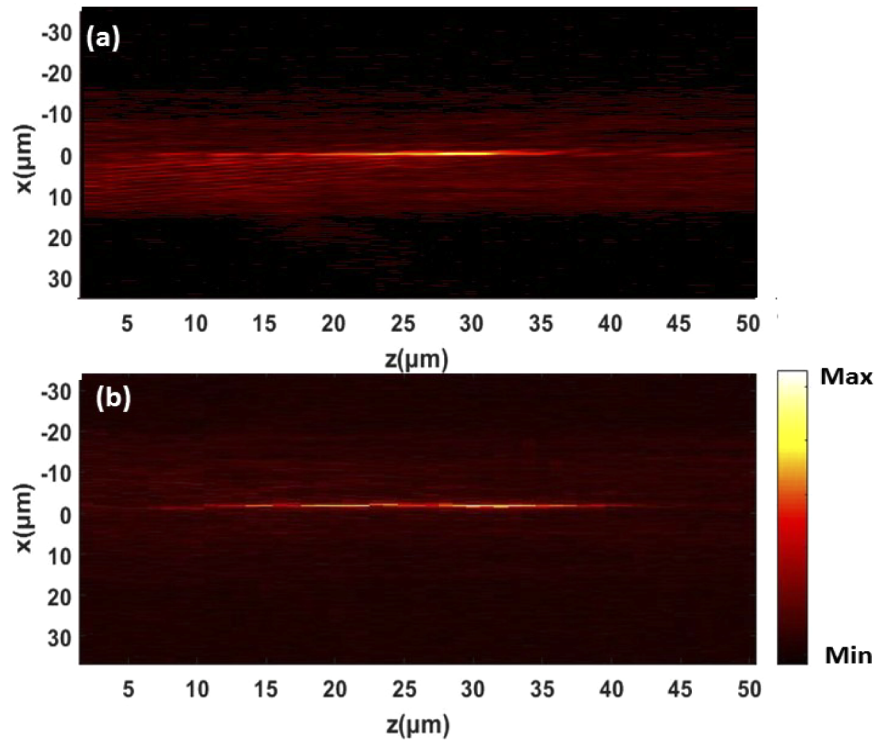
According to the geometric optics, we can know that the propagation distance of the SHG Bessel beam can be obtained by the following formula [17],

$$Z_{\max} = \frac{R}{\tan \alpha} \quad (7)$$

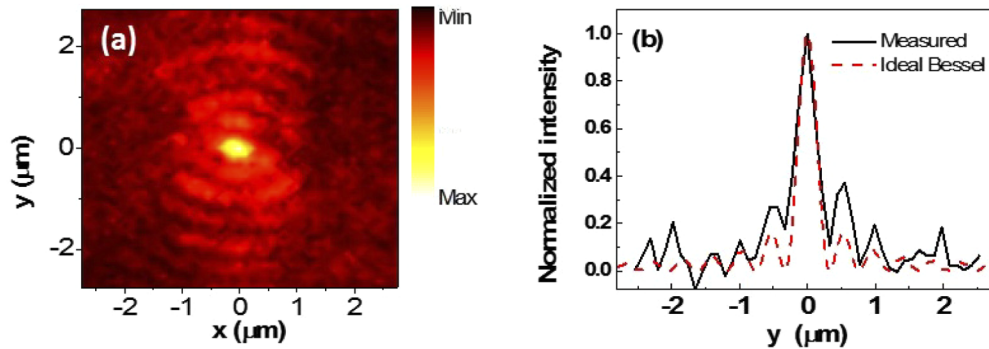
In our experiments, the angle  $\alpha$  is  $26.7^\circ$ , so we can get the theoretical value of  $Z_{\max}$  is  $29 \mu\text{m}$  and  $39 \mu\text{m}$  for the two nonlinear meta-axicons with  $R = 15 \mu\text{m}$  and  $R = 20 \mu\text{m}$ , respectively. From Figs. 5(a) and 5(b), we can obtain the experimental results of the  $Z_{\max}$  are about  $31 \mu\text{m}$  and  $40 \mu\text{m}$ , respectively. The experimental results is close to the theoretical values. A larger propagation distance of Bessel beam could also be generated, by using a bigger metasurface.

Figure 6(a) shows the intensity distribution in  $xy$  cut planes at the distance of  $z = 28 \mu\text{m}$ . We can see in the plane, the light power are constrained mostly at the center spot whereas the side lobes are much weaker, which is an obvious characteristic of the zero-order Bessel beam. Figure 6(b) shows the corresponding intensity distribution along  $y$  axis in the plane. From this figure, we clearly observe the Bessel-like distribution in the transverse direction, in which the curve is fitted by the first kind Bessel function well. The above measured results demonstrate that spatial zero-order Bessel beams of SHG are generated by the hybrid nonlinear metasurface.

The full width at half maximum (FWHM) of the zero-order Bessel beam is defined as the waist. According to the references, FWHM of zero-order Bessel beam can be calculated by the



**Fig. 5.** Electric field intensity profile in  $xz$  plane of SHG for the zero-order Bessel beam hybrid metasurfaces with (a)  $R = 15 \mu\text{m}$  and (b)  $R = 20 \mu\text{m}$ , respectively.



**Fig. 6.** (a) SHG intensity distributions in the  $xy$  plane at  $z = 28 \mu\text{m}$ . (b) The SHG intensity distribution along  $x = 0$  in the  $xy$  plane. The dotted curve is the results of Bessel function fitting.

followed equation [17],

$$FWHM = \frac{0.358\lambda_{SHG}}{\sin \alpha} \quad (8)$$

We calculate the FWHM of the zero-order nonlinear Bessel beam by the above formula. It is 319 nm. From Fig. 6(b) we can see the FWHM of the zero-order nonlinear meta-axicon is about 330 nm, close to the theoretical value. The difference of FWHM between the calculated results and the experimental results is mostly attributed to the limit of the imaging system resolution and the errors induced in the measurement operation.

The nonlinear metasurface with  $R = 20 \mu\text{m}$  to generate nonlinear first-order Bessel beam is also fabricated. Figures 7(a) and 7(b) show the longitudinal and transverse SHG intensity distribution obtained with the nonlinear first-order Bessel beam generator. Unlike the zero-order Bessel beam, the first-order Bessel beam has a ring-like magnitude distribution. The first-order beam is non-diffracting until a certain distance. It can be seen that the most of the power is contained in the main lobe whereas the side lobes are sufficiently weaker. However, we can see that the ring is not perfect, and some bright spots occurred in the ring. We attribute this un-uniform magnitude distribution mainly to the space-variant polarization states.

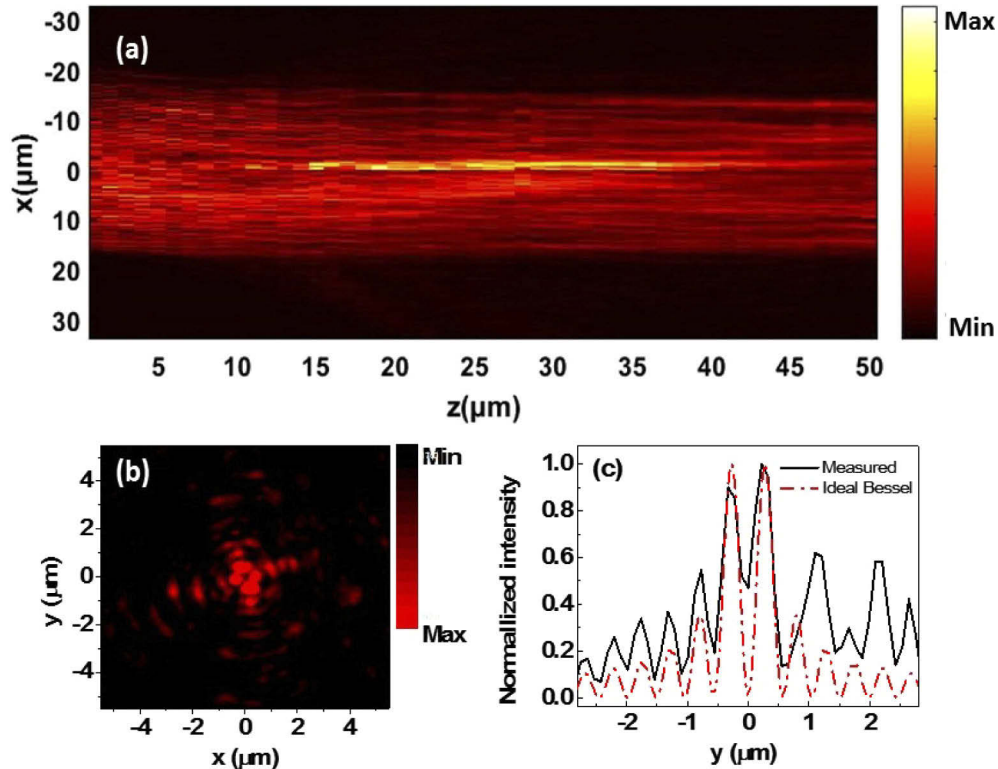


**Fig. 7.** (a) Electric field intensity profile in  $xz$  plane of SHG for the first-order Bessel beam hybrid metasurface with  $R = 20 \mu\text{m}$ . (b) SHG intensity distributions in the  $xy$  plane at  $z = 25 \mu\text{m}$ . (c) The SHG intensity distribution along  $x = 0$  in the  $xy$  plane. The dotted curve is the results of Bessel function fitting.

Though the obtained SHG Bessel profiles for the first-order Bessel beam does not form perfect ring, this is not the case for the zero-order Bessel beam. The reason is that the metasurface of zero-order Bessel beam has only radial phase variations and is symmetrical, whereas the metasurface for the first-order Bessel beam has variations in both the radial and azimuthal directions. In fact, due to the real spatially varying intensity of  $E_x$  and  $E_y$  of the incident light, the Bessel beams are not homogeneously polarized, which also can be observed in linear Bessel beams [17–18]. And compared with the linear Bessel meta-axicon, the un-uniform distribution of SHG Bessel beam is even more seriously due to the second order effects. Furthermore, for different oriented holes, the space-variant polarization states will induce un-uniform enhancement effects of SHG, which will exacerbate un-uniform distribution of the magnitude. According to the results of Fig. 4, the local field enhancement of unit cells with different oriented nanoholes are not the same. So differences of the enhancement effects can influence the intensity distribution of SHG even under the ideal

circular polarized light excitation, which can contribute to the non-uniform field distributions along the angle direction. Finally, the defects and the misalignment of the nanoholes introduced in the fabrication lead to more seriously un-uniform magnitude distribution.

The transverse intensity distribution along  $y$  axis is shown in Fig. 7(c). We can see the curve is fitted by first-order Bessel function well. The FWHM for the first-order Bessel beam is defined as twice the distance from the center dark spot to the closest point on the ring at the half of the maximum intensity. The theoretical FWHM can be calculated by the followed equation [17],

$$FWHM = \frac{0.292\lambda_{SHG}}{\sin \alpha} \quad (9)$$

Then the FWHM can be calculated to be 260 nm. From Fig. 7, we can see the experimental value of FWHM of the first-order Bessel beam is about 250 nm, which is close to the theoretical value. The agreement between the experimental and theoretical results demonstrates the new type of nonlinear hybrid meta-axicon is able to realize miniaturized nonlinear optical devices related to generate Bessel beams, which have potential application in nonlinear optical manipulation, imaging and tractor beams.

## 5. Conclusion

In conclusion, we present a type of nonlinear meta-axicon to generate SHG Bessel beams. The nonlinear metasurfaces are consistent of a gold metasurface coupled to a monolayer  $WS_2$ . The hybrid nonlinear meta-axicon can realize modulation of electronic field and frequency conversion simultaneously. Zero-order and first-order Bessel beams of second harmonic are generated. The non-diffracting distance and FWHM of the second harmonic Bessel beams are analyzed theoretically and experimentally. The experimental results are close to the theory predicted results, realizing of miniaturized nonlinear meta-axicons, which have potential applications in nonlinear optical manipulation, imaging and tractor beams.

## Funding

National Natural Science Foundation of China (11004067, 11774115, 91850113); National Basic Research Program of China (973 Program) (2014CB921301); Doctoral Program Foundation of Institutions of Higher Education of China (20130142110078).

## Acknowledgments

We thank the Center of Nano-Science and Technology of Wuhan University for their support of sample fabrication. Special thanks to the Analytical and Testing Center of HUST and the Center for Nanoscale Characterization & Devices (CNCD) of WNLO for using their facilities.

## Disclosures

The authors declare no conflicts of interest.

## References

1. J. V. Carrión, J. Albero, M. Baranski, C. Gorecki, and N. Passilly, "Microfabrication of axicons by glass blowing at a wafer-level," *Opt. Lett.* **44**(13), 3282–3285 (2019).
2. S. Chowdhury, R. P. Roberts, G. Molina-Terriza, and X. Vidal, "Lens-axicon separation to tailor aberration free focused Bessel-Gaussian beams in the paraxial regime," *Opt. Express* **27**(8), 11160–11171 (2019).
3. C. Holmes and P. G. R. Smith, "Self-assembled axicon lens in integrated optical fiber," *Opt. Lett.* **44**(14), 3506–3509 (2019).
4. Y. Zhu, D. Wei, Z. Kuang, Q. Wang, Y. Wang, X. Huang, Y. Zhang, and M. Xiao, "Broadband Variable Meta-Axicons Based on Nano-Aperture Arrays in a Metallic Film," *Sci. Rep.* **8**(1), 11591 (2018).

5. V. Pyragaite, A. Piskarskas, K. Regelskis, V. Smilgevicius, A. Stabinis, and S. Mikalauskas, "Parametric down-conversion of higher-order Bessel optical beams in quadratic nonlinear medium," *Opt. Commun.* **240**(1-3), 191–200 (2004).
6. I. Manek, Y. B. Ovchinnikov, and R. Grimm, "Generation of a hollow laser beam for atom trapping using an axicon," *Opt. Commun.* **147**(1-3), 67–70 (1998).
7. C. Pfeiffer and A. Grbic, "Controlling Vector Bessel Beams with Metasurfaces," *Phys. Rev. Appl.* **2**(4), 044012 (2014).
8. S. Liu, A. Noor, L. L. Du, L. Zhang, Q. Xu, K. Luan, T. Q. Wang, Z. Tian, W. X. Tang, J. G. Han, W. L. Zhang, X. Y. Zhou, Q. Cheng, and T. J. Cui, "Anomalous Refraction and Nondiffractive Bessel-Beam Generation of Terahertz Waves through Transmission-Type Coding Metasurfaces," *ACS Photonics* **3**(10), 1968–1977 (2016).
9. T. Li, X. B. Hu, H. M. Chen, C. Zhao, Y. Xu, X. Wei, and G. F. Song, "Metallic metasurfaces for high efficient polarization conversion control in transmission mode," *Opt. Express* **25**(20), 23597–23604 (2017).
10. Q. H. Ke, Y. M. Zhou, J. Tan, M. R. He, J. T. Liang, Y. Zhao, M. Li, and P. X. Lu, "Two-dimensional photoelectron holography in strong-field tunneling ionization by counter rotating two-color circularly polarized laser pulses," *Opt. Express* **27**(22), 32193–32209 (2019).
11. A. Arbabi, Y. Horie, M. Bagheri, and A. Faraon, "Dielectric metasurfaces for complete control of phase and polarization with subwavelength spatial resolution and high transmission," *Nat. Nanotechnol.* **10**(11), 937–943 (2015).
12. B. N. Wang, L. X. He, Y. Q. He, Y. F. Zhang, R. Z. Shao, P. F. Lan, and P. X. Lu, "All-optical measurement of high-order fractional molecular echoes by high-order harmonic generation," *Opt. Express* **27**(21), 30172–30181 (2019).
13. N. M. Estakhri and A. Alù, "Recent progress in gradient metasurfaces," *J. Opt. Soc. Am. B* **33**(2), A21–A30 (2016).
14. P. Genevet, F. Capasso, F. Aieta, M. Khorasaninejad, and R. Devlin, "Recent advances in planar optics: from plasmonic to dielectric metasurfaces," *Optica* **4**(1), 139–152 (2017).
15. M. R. Akram, M. Q. Mehmood, X. Bai, R. Jin, M. Premaratne, and W. Zhu, "High efficiency ultrathin transmissive metasurfaces," *Adv. Opt. Mater.* **7**(11), 1801628 (2019).
16. H. Gao, M. Pu, X. Li, X. Ma, Z. Zhao, Y. Guo, and X. Luo, "Super-resolution imaging with a Bessel lens realized by a geometric metasurface," *Opt. Express* **25**(12), 13933 (2017).
17. W. T. Chen, M. Khorasaninejad, A. Y. Zhu, J. Oh, R. C. Devlin, A. Zaidi, and F. Capasso, "Generation of wavelength-independent subwavelength Bessel beams using metasurfaces," *Light: Sci. Appl.* **6**(5), e16259 (2017).
18. M. R. Akram, M. Q. Mehmood, T. Tauqeer, A. S. Rana, I. D. Rukhlenko, and W. Zhu, "Highly efficient generation of Bessel beams with polarization insensitive metasurfaces," *Opt. Express* **27**(7), 9467 (2019).
19. W. Wei, X. Jiang, L. Dong, W. Liu, X. Han, Y. Qin, K. Li, W. Li, Z. Lin, and P. Lu, "Regulating second-harmonic generation by Van der Waals Interactions in 2D lead halide perovskite nanosheets," *J. Am. Chem. Soc.* **141**(23), 9134–9139 (2019).
20. Z. Yang, W. Cao, X. Chen, J. Zhang, Y. Mo, H. Xu, K. Mi, Q. Zhang, P. Lan, and P. Lu, "All-optical frequency resolved optical gating for isolated attosecond pulse reconstruction," *Opt. Lett.* **45**(2), 567–570 (2020).
21. W. Zang, Z. Qin, X. Yang, Z. Chen, S. Wang, and Z. Wang, "Polarization Generation and Manipulation Based on Nonlinear Plasmonic Metasurfaces," *Adv. Opt. Mater.* **7**, 1801747 (2019).
22. M. Ren, W. Cai, and J. Xu, "Tailorable Dynamics in Nonlinear Optical Metasurfaces," *Adv. Mater.* 1806317 (2019).
23. M. Kauranen and A. V. Zayats, "Nonlinear plasmonics," *Nat. Photonics* **6**(11), 737–748 (2012).
24. J. Butet, P. F. Brevet, and O. J. Martin, "Optical second harmonic generation in plasmonic nanostructures: From fundamental principles to advanced applications," *ACS Nano* **9**(11), 10545–10562 (2015).
25. J. Lee, M. Tymchenko, C. Argyropoulos, P. Y. Chen, P. Y. Lu, F. Demmerle, G. Boehm, M. C. Amann, A. Alu, and M. A. Belkin, "Giant nonlinear response from plasmonic metasurfaces coupled to intersubband transitions," *Nature* **511**(7507), 65–69 (2014).
26. R. Sarma, D. Ceglie, N. Nookala, M. A. Vincenti, S. Campione, O. Wolf, M. Scalora, M. B. Sinclair, M. A. Belkin, and I. Brener, "Broadband and Efficient Second-Harmonic Generation from a Hybrid Dielectric Metasurface/Semiconductor Quantum-Well Structure," *ACS Photonics* **6**(6), 1458–1465 (2019).
27. Y. L. Song, W. W. Liu, C. Fang, L. H. Li, and P. X. Lu, "Enhanced optoelectronic performance of 2D organic-inorganic hybrid perovskite through light-illumination," *Opt. Express* **27**(21), 30618–30628 (2019).
28. J. W. Chen, K. Wang, H. Long, X. B. Han, H. B. Hu, W. W. Liu, B. Wang, and P. X. Lu, "Tungsten disulfide–gold nanohole hybrid metasurfaces for nonlinear metalenses in the visible region," *Nano Lett.* **18**(2), 1344–1350 (2018).
29. N. Kumar, S. Najmaei, Q. Cui, F. Ceballos, P. M. Ajayan, J. Lou, and H. Zhao, "Second harmonic microscopy of monolayer MoS<sub>2</sub>," *Phys. Rev. B* **87**(16), 161403 (2013).
30. C. Janisch, Y. Wang, D. Ma, N. Mehta, A. L. Elías, N. Perea-López, M. Terrones, V. Crespi, and Z. Liu, "Extraordinary second harmonic generation in Tungsten Disulfide monolayers," *Sci. Rep.* **4**(1), 5530 (2015).
31. G. W. Hu, X. M. Hong, K. Wang, W. J. Wang, H. X. Xu, W. C. Zhao, W. W. Liu, S. Zhang, F. Garcia-Vidal, B. Wang, P. X. Lu, and C. W. Qiu, "Coherent steering of nonlinear chiral valley photons with a synthetic Au–WS<sub>2</sub> metasurface," *Nat. Photonics* **13**(7), 467–472 (2019).
32. N. Yu, P. Genevet, M. A. Kats, F. Aieta, J. P. Tetienne, F. Capasso, and Z. Gaburro, "Light Propagation with Phase Discontinuities: Generalized Laws of Reflection and Refraction," *Science* **334**(6054), 333–337 (2011).

33. X. H. Li, W. W. Liu, Y. L. Song, H. Long, K. Wang, B. Wang, and P. Lu, "Two-photon-pumped high-quality, single-mode vertical cavity lasing based on perovskite monocrystalline films," *Nano Energy* **68**, 104334 (2020).
34. X. H. Li, W. W. Liu, Y. L. Song, C. Zhang, H. Long, K. Wang, B. Wang, and P. X. Lu, "Enhancement of the second harmonic generation from WS<sub>2</sub> monolayers by cooperating with dielectric microspheres," *Adv. Opt. Mater.* **7**(3), 1801270 (2019).
35. N. M. Jassim, K. Wang, X. Han, H. Long, B. Wang, and P. X. Lu, "Plasmon assisted enhanced second-harmonic generation in singlehybrid Au/ZnS nanowires," *Opt. Mater.* **64**, 257–261 (2017).